Bioactive Materials 24 (2023) 463–476

Contents lists available at ScienceDirect

Bioactive Materials

journal homepage: www.keaipublishing.com/en/journals/bioactive-materials

Intelligent microneedle patch with prolonged local release of hydrogen and magnesium ions for diabetic wound healing

Pei Wang [a,1], Jiayingzi Wu [b,1], Haiyan Yang [c], Hengke Liu [b], Tianyu Yao [c], Chang Liu [a], Yan Gong [a], Mingsong Wang [a], Guangyu Ji [a], Peng Huang [b,*], Xiansong Wang [a,**]

[a] Department of Thoracic Surgery, Shanghai Key Laboratory of Tissue Engineering, Shanghai Ninth People's Hospital, Shanghai Jiao Tong University School of Medicine, Shanghai, 200011, China
[b] Marshall Laboratory of Biomedical Engineering, International Cancer Center, Laboratory of Evolutionary Theranostics (LET), School of Biomedical Engineering, Shenzhen University Medical School, Shenzhen, 518060, China
[c] Center of Hydrogen Science, Shanghai Jiao Tong University, Shanghai, 200240, China

ARTICLE INFO

Keywords:
Microneedle patch
Magnesium hydride
Hydrogen
Magnesium ion
Diabetic wound healing

ABSTRACT

Diabetes mellitus, an epidemic with a rapidly increasing number of patients, always leads to delayed wound healing associated with consistent pro-inflammatory M1 polarization, decreased angiogenesis and increased reactive oxygen species (ROS) in the microenvironment. Herein, a poly (lactic-*co*-glycolic acid) (PLGA)-based microneedle patch loaded with magnesium hydride (MgH_2) (MN-MgH_2) is manufactured for defeating diabetic wounds. The application of microneedle patch contributes to the transdermal delivery and the prolonged release of MgH_2 that can generate hydrogen (H_2) and magnesium ions (Mg^{2+}) after reaction with body fluids. The released H_2 reduces the production of ROS, transforming the pathological microenvironment induced by diabetes mellitus. Meanwhile, the released Mg^{2+} promotes the polarization of pro-healing M2 macrophages. Consequently, cell proliferation and migration are improved, and angiogenesis and tissue regeneration are enhanced. Such intelligent microneedle patch provides a novel way for accelerating wound healing through steadily preserving and releasing of H_2 and Mg^{2+} locally and sustainably.

1. Introduction

The population diagnosed with diabetes has seen a mounting prevalence in the past decades [1], and the mortality and disability concerning diabetes are experiencing an astounding increase [2–5]. Diabetic foot ulcer (DFU) is one of the most common risks of complications, affecting 15–25% of patients with diabetes mellitus [6]. Particularly, hyperglycemic microenvironment including consistent pro-inflammatory M1 macrophage polarization [7,8], deteriorating blood vessels [9–11] and accumulated reactive oxygen species (ROS) [12–14] resulting from diabetes mellitus would delay the wound healing process and even lead to gangrene amputation [15]. Despite recent developments in hypoglycemic drugs [16], glucose monitoring techniques and insulin pumps [17], only limited approaches have been established to manage the hyperglycemic microenvironment of diabetic wounds. Therefore, new treatments aiming to enhance pro-healing M2 macrophage polarization and angiogenesis and to reduce ROS production in the hyperglycemic microenvironment are in urgent need for accelerating diabetic wound healing.

Hydrogen (H_2) has been proved to be therapeutic effective and non-cytotoxic. H_2 as an antioxidant is capable of resisting the oxidative stress posed on tissue and cells without disturbing normal metabolic oxidation or cell signaling system [18]. With its efficacy in reducing ROS production, H_2 would be a promising therapeutic agent to alter the inflammatory microenvironment induced by diabetes mellitus. Previously, the inhalation of H_2 has been applied as an antioxidant therapy for treating brain injury [18], vascular diseases, and cancers [19]. However, H_2 is characterized by high diffusivity, low aqueous solubility and dose-dependent effect [20], leading to the limited therapeutic efficacy of inhalation therapy. To overcome these challenges,

Peer review under responsibility of KeAi Communications Co., Ltd.
* Corresponding author.
** Corresponding author.
E-mail addresses: peng.huang@szu.edu.cn (P. Huang), wonderluis@126.com (X. Wang).
[1] These authors contributed equally to this work.

https://doi.org/10.1016/j.bioactmat.2023.01.001
Received 2 October 2022; Received in revised form 4 December 2022; Accepted 2 January 2023

stimuli-responsive nanomaterials, such as photoactivated nanocatalysts [21–23] and acid-responsive H_2 prodrugs [24,25], were developed for site-specific delivery and release of H_2 with enhanced therapeutic efficacy through subcutaneous or intravenous injection. Yet, it is still difficult to achieve long-term release of H_2 for the optimal therapeutic impact.

Magnesium (Mg) metal, as a strong reductive metal, could react with H_2O and spontaneously generate H_2 gas. Mg and its alloys have been widely used as biodegradable implants for tissue repair/regeneration in clinics, but only until recently have researchers utilized their H_2 generation capability for disease treatments [26]. For example, poly (lactic-*co*-glycolic acid) (PLGA) microparticles containing Mg powder were intra-muscularly close to the osteoarthritis knee to tackle inflammation through H_2 therapy [27]. Nevertheless, the reaction rate between Mg and H_2O is relatively slow, leading to the insufficient H_2 evolution. Meanwhile, Mg powder is intrinsically flammable [28], which raises safety concerns during the sample preparation process. In a most recent work, researchers reported a Mg-based galvanic cell made by decorating platinum on the surface of Mg rods for H_2 therapy of cancer [29]. Such galvanic cell could generate H_2 more efficiently than Mg powder. However, as a medical device, it needed to be implanted into the lesions, which might cause surgical risks including implantation failure, infection, and pain.

Herein, we developed a PLGA-based microneedle patch loaded with magnesium hydride (MgH_2) macroparticles (MN-MgH_2) for transdermal delivery and prolonged release of H_2 and Mg ions (Mg^{2+}) for treating diabetic wounds in a minimally invasive manner (Fig. 1). MgH_2 is a conventional H_2 storage material for mobile applications. Compared to Mg powder, MgH_2 can store/generate a larger amount of H_2 and is much more stable at room temperature. However, the application of MgH_2 in H_2 therapy has been rarely explored yet. Moreover, the resulted Mg^{2+} could facilitate macrophages phenotype alteration [30–32] into pro-healing M2 macrophages and enhance angiogenesis [33] for attenuating microvascular lesions caused by the hyperglycemic microenvironment. Thus, MgH_2 potentially could be a promising therapeutic agent for diabetic wound healing. Meanwhile, as the subcutaneous drug delivery efficacy of microneedle patches has been widely demonstrated before [34,35], the usage of PLGA-based microneedle patch also enables transdermal delivery of MgH_2 with minimal invasiveness, protects MgH_2 from contacting water to prolong its lifetime and allows sustainable release of MgH_2 into the physiological microenvironment. Additionally, the dissolved PLGA and its degradation products (lactic acid and glycolic acid) increased the local acidity and thus promote the release of Mg^{2+} from $Mg(OH)_2$. As a result, the enhanced wound healing process with reduced ROS production, promoted M2 polarization, enhanced cell proliferation and migration, as well as improved angiogenesis and tissue regeneration were achieved both in vitro and *in vivo* by applying MN-MgH_2.

2. Results and discussion

2.1. Synthesis and characterizations of MN-MgH_2

MgH_2 was loaded into a PLGA-based microneedle patch for protecting it from water and realizing slow-releasing of H_2 and Mg^{2+}. Briefly, MgH_2 was immersed in 1, 4-dioxane together with PLGA to fabricate MN-MgH_2 (Fig. 2a). The microneedle patch containing only PLGA, as a control material, was also fabricated and named as MN-PLGA. MgH_2 was synthesized through plasma-assisted evaporation combined with in-situ hydrogenation technology. ICP-MS was applied for testing the MgH_2 purity which proved that the content of Mg element reached 99.9% (Fig. S1). Meanwhile, SEM images revealed the relatively uniformed spherical morphology of MgH_2 with an average diameter of 8.1 μm (Fig. 2b). XRD was utilized to further verify the high purity of MgH_2, and the result confirmed that MgH_2 possessed a rather high degree of crystallinity with quite a small percentage of it being Mg (Fig. 2c). In addition, thermogravimetric (TG) and differential scanning calorimetry (DSC) characterizations of MgH_2 were also carried out to investigate its chemical stability. Results of both TG and DSC indicated that MgH_2 remained stable until the temperature reached above 403 °C (Fig. 2d), which ensured that the fabrication process (40 °C) of MN-MgH_2 would not change the characteristics of MgH_2. Fig. 2e demonstrated the photographic image of MN-MgH_2 which was composed of a 10 × 10 array. Furthermore, SEM images of MN-MgH_2 from different angles and under different magnifications revealed the rectangular pyramid shape of the needle tips with a 200 μm × 200 μm × 500 μm (W × L × H) dimensions. Photographic and confocal images of MN-PLGA were also presented in Fig. S2, which showed the same dimensions as

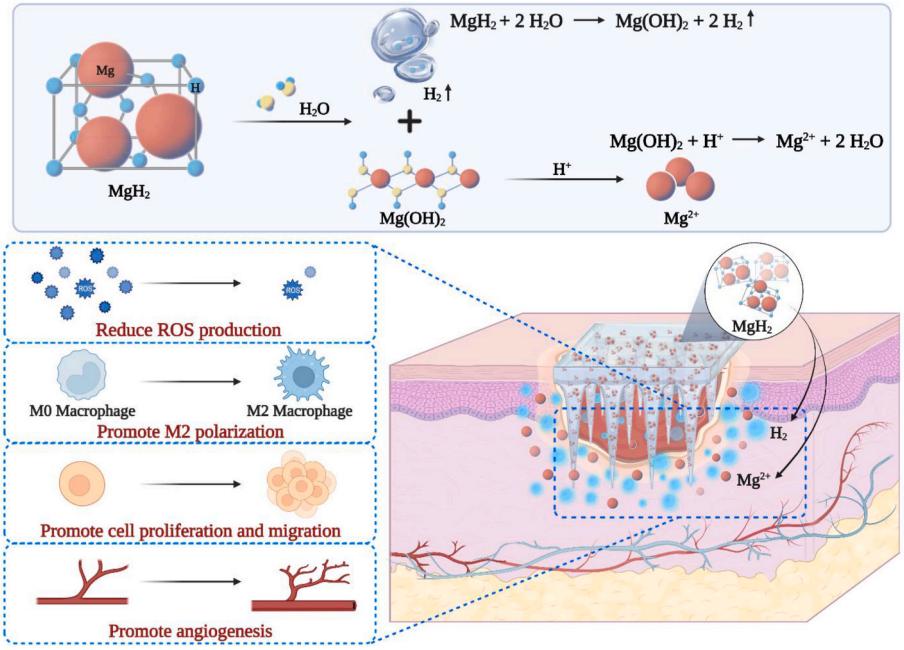

Fig. 1. Schematic illustration of microneedle patch containing MgH_2 (denoted as MN-MgH_2) and its functional mechanism.

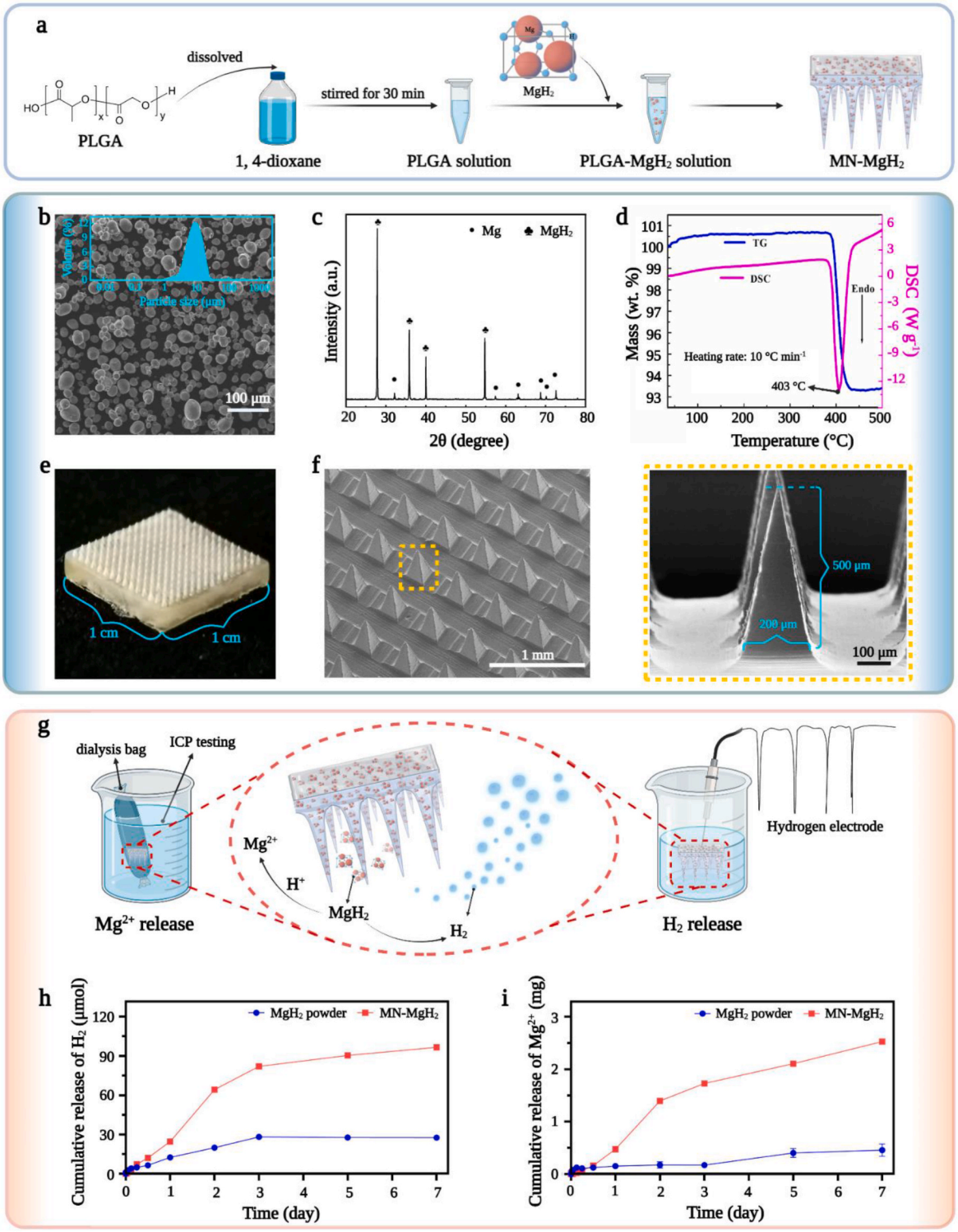

Fig. 2. Synthesis and characterizations of MgH_2, MN-PLGA and MN-MgH_2. a) Schematic illustration of the fabrication process of MN-MgH_2. b) SEM images of MgH_2 with its particle size analysis. c) XRD results of Mg and MgH_2. d) TG and DSC results of MgH_2. e) Photographic images of MN-MgH_2. f) SEM images of MN-MgH_2 under different magnifications. g) Schematic illustration of the test methods for measuring Mg^{2+} and H_2 released from MN-MgH_2. h) Release profiles of H_2 from MgH_2 powder and MN-MgH_2 immersed in pure water (pH = 7). i) Release profiles of Mg^{2+} from MgH_2 powder and MN-MgH_2 immersed in pure water (pH = 7).

the MN-MgH_2.

After successfully fabricating the MN-MgH_2, the release profiles of H_2 and Mg^{2+} from MgH_2 powder and MN-MgH_2 were studied (Fig. 2g). When being immersed in pure water, the MN-MgH_2 produced 3.50 times more H_2 than the MgH_2 powder on day 7 under the same experimental condition (Fig. 2h). Meanwhile, the amount of free Mg^{2+} generated by the MN-MgH_2 was 5.52 times more than that by the MgH_2 powder on day 7 (Fig. 2i). We hypothesized that the hydrolysis reaction of MgH_2 was hindered by the formation of a $Mg(OH)_2$ layer on the surface of MgH_2 particles, while the PLGA and its acidic degradation products in MN-MgH_2 was able to dissolve the $Mg(OH)_2$ layer and thus accelerated the H_2 as well as the soluble Mg^{2+} generation ($MgH_2 + H_2O \rightarrow Mg(OH)_2$

+ H_2, $Mg(OH)_2 + H^+ \rightarrow Mg^{2+} + H_2O$). To validate our hypothesis, we first demonstrated that the hydrolysis of PLGA in water indeed led to a significant pH decrease (Fig. S3a). Then, we further investigated the effect of pH on the H_2 production by putting MgH_2 powders in different pH solutions (Fig. S3b). It is found that the amount of H_2 increased as the pH value decreased, indicating that the acidic pH facilitated the H_2 production. Next, we characterized the formation of the $Mg(OH)_2$ layer on MgH_2 particles. According to the elemental mapping results, the pristine MgH_2 contained negligible oxygen (O) element but after reacting with water for 7 days there was noticeable O on MgH_2 particles, confirming the formation of $Mg(OH)_2$ layer (Fig. S3c). Last but not the least, after hydrolysis the particle size of MgH_2 in the microneedle was much smaller than that of the MgH_2 powder in water, which also supported the hypothesis that the PLGA destructed the Mg $(OH)_2$ layer and facilitated the reaction between MgH_2 and water (Fig. S3d). Collectively, we have proven that enhanced production of H_2 and soluble Mg^{2+} are likely due to the presence of PLGA which resulted in an acidic environment.

2.2. MN-MgH_2 reduced ROS production in vitro

After validating the advantage of MN-MgH_2 in the prolonged release of H_2, we then studied whether it could enable ROS reduction in vitro. First, lipopolysaccharide (LPS) was added into one well of Raw264.7 cells to induce ROS overproduction, and cells were seeded in 6-well-plates and cocultured with MN-PLGA extract, MN-MgH_2 extract, MgH_2 solution (1 μg mL^{-1}) or normal cell culture medium (control group). After cocultivation for 24 h, Raw264.7 cells were stained with ROS staining assay (DCFH-DA, in green) and then imaged with a fluorescence microscope. The representative images of each group demonstrated that the application of MgH_2 solution or MN-MgH_2 extract noticeably decreased ROS levels, and the MN-MgH_2 extract led to the most obvious ROS reduction (Fig. 3a). To quantify the decline in ROS production, the stained Raw264.7 cells were collected for flow cytometry analysis (Fig. 3b). The data obtained from flow cytometry was quantified and presented in Fig. 3c. The results showed that MgH_2 solution and MN-MgH_2 extract reduced the production of ROS to 70.77% and 50.24%, respectively, confirming the superiority of MN-MgH_2 in reducing ROS levels.

2.3. MN-MgH_2 induced M2 polarization in vitro

After validating the advantages of MN-MgH_2 in ROS reduction through H_2 therapy, we then studied its function in inducing macrophage cellular phenotype alteration due to the release of Mg^{2+}. In contrast to the control (no treatment) or MN-PLGA extract-treated Raw264.7 cells, the SEM images showed that cells treated with MgH_2 solution (1 μg mL^{-1}) or MN-MgH_2 extract developed unambiguous morphologies (Fig. 3d), indicating the Mg^{2+} induced polarization of macrophages. For a more detailed investigation, real-time RT-PCR (RT-qPCR) was performed with Raw264.7 cells that treated MN-MgH_2 extract for 24 h. Cells without any treatment were applied as the control group. The expressions of M1 macrophages biomarkers (IL-6, IL-1β, iNOS) and M2 macrophages biomarkers (Arg-1) at mRNA level were evaluated through RT-qPCR (Fig. 3e). The results show that the expression of IL-6, IL-1β and iNOS had statistically significant decreases in MN-MgH_2 extract groups, proving that the polarization to M1 was suppressed after the treatments. While the expression of Arg-1 was significantly increased in MN-MgH_2 extract group, indicating the simultaneously increased M2 repolarization after the treatments. The primer sequences used in RT-qPCR were summarized in Fig. S4. In conclusion, MN-MgH_2 facilitated the polarization of pro-inflammatory M1 macrophages into the pro-healing M2 macrophages.

2.4. MN-MgH_2 enhanced cell proliferation and migration in vitro

CCK-8 assay was used to investigate the impacts of MgH_2 and MN-MgH_2 on cell viability and proliferation. Fig. 4a demonstrated that after 72 h-treatment, the cell viability of fibroblasts had no significant difference between the MN-PLGA extract group and the control group, while there was a statistically significant increase in MN-MgH_2 extract group, indicating that MN-PLGA had no noticeable cytotoxicity to fibroblasts while MN-MgH_2 would further promote the proliferation of fibroblasts. Meanwhile, the optimal concentration of MgH_2 for the proliferation of fibroblasts was determined to be 1 μg mL^{-1} (Fig. 4b). Therefore, 1 μg mL^{-1} MgH_2 solution was used in the following experiments unless otherwise mentioned. Besides, the results were also confirmed by live/dead double staining experiments, and similar conclusions were obtained (Fig. S5).

Then, the impact of MN-MgH_2 on cell migration capability was studied. The nuclei of migrated HUVECs were stained with Hoechst, and the representative confocal images were presented in Fig. 4c. Quantitatively, there was no difference be between the MN-PLGA extract and control group, but there was a significant increase in cell mobility after treatment of MgH_2 solution or MN-MgH_2 extract (Fig. 4d). Particularly, the cell mobility of MN-MgH_2 extract group was 1.30 times higher than that of MgH_2 solution, which was likely due to the higher Mg^{2+} generation. Furthermore, the cell migration capability of fibroblasts was also evaluated using an in vitro wound healing scratch assay. The promoted wound closure was observed by using MgH_2 solution or MN-MgH_2 extract (Fig. 4e). Quantitatively, the gap closure ratio of the MgH_2 solution and MN-MgH_2 extract group was 1.28-fold and 1.94-fold higher than that of the control group, respectively (Fig. 4f). In addition, the tube formation experiment was performed (Fig. 4g). HUVECs were incubated with either normal cell culture medium (control group), or MgH_2 solution or MN-MgH_2 extract for 4 h. Nodes and tube lengths of different groups were quantified and presented in Fig. 4h. The treatment of MN-MgH_2 extract improved the nodes and tube length by 3.54-fold and 2.22-fold. Taken together, the advantage of MN-MgH_2 for promoting cell proliferation and migration was validated in vitro, and it is expected to promote angiogenesis and tissue regeneration *in vivo*.

2.5. MN-MgH_2 promoted wound healing in vivo

The *in vivo* wound healing efficacy of MN-MgH_2 was further evaluated on living diabetic mice bearing cutaneous wounds (Fig. 5a). Basically, the mouse model was established by creating 6 mm round wounds on the back of diabetic (db/db) mice. After the surgery, all mice were randomly divided into 3 groups which were applied with PBS (control group), MgH_2 powder or MN-MgH_2. The morphology of the MN-MgH_2 after insertion was recorded over time (Fig. S6), and it shows that the patch became whiter and more and more small bubbles appeared on MN-MgH_2 over time, as H_2 gas was released. Meanwhile, photographic images of the wound area on mice with different treatments were taken on day 0, 3, 5, 7, 10, 12, and 14 (Fig. 5b). On day 10, wounded areas of mice in the MN-MgH_2 group had almost healed, while the wounds in the other groups remained unhealed. The percentages of wound areas on different days were quantified with Image J (Fig. 5c). Compared to the control group and MgH_2 powder group, MN-MgH_2 group demonstrated a statistically significant improvement in minimizing the wound areas.

2.6. MN-MgH_2 reduced ROS production in vivo

The ROS reduction efficacy of MgH_2 was tested *in vivo* through ROS staining. Skin samples of diabetic mice in different groups were taken on day 3 and 7, and was stained with dihydroethidium dye (DHE, in red). The representative images of different groups at different time points were presented in Fig. 6a. The fluorescence intensity quantification result obtained on day 3 demonstrated that the treatment of MgH_2 powder and MN-MgH_2 decreased the ROS production by 1.65-fold and

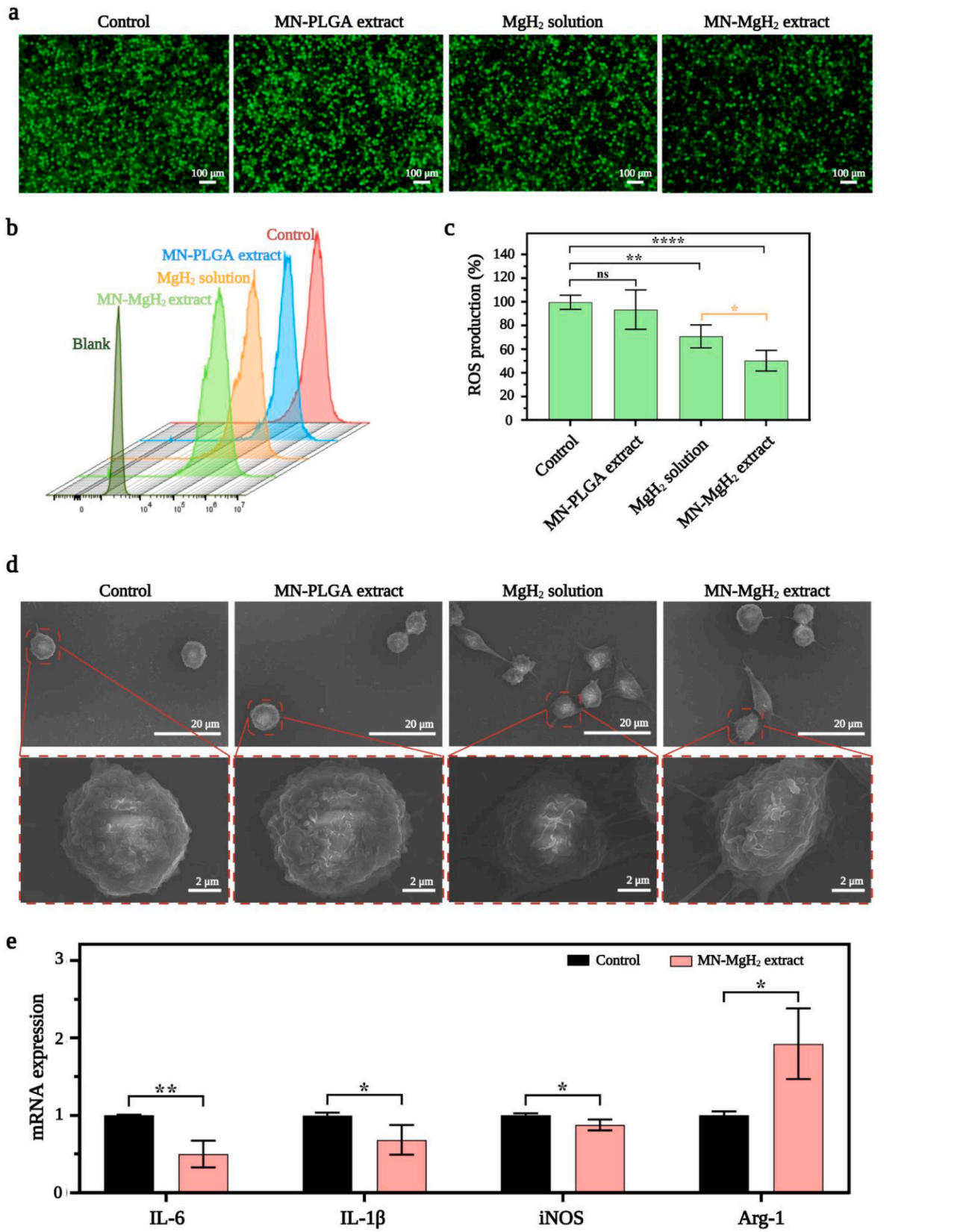

Fig. 3. *In vitro* ROS reduction and M2 polarization induced by MN-MgH_2. a) ROS assay of Raw264.7 cells after 24-h treatment with MN-PLGA extract, MN-MgH_2 extract, MgH_2 solution or normal cell culture medium (control group). ROS was stained with DCFH-DA (green). b) Flow analysis of ROS fluorescence staining of Raw264.7 cells after different treatments. c) Statistic analysis of ROS production in each group. d) SEM images of Raw264.7 cells polarization after 24-h treatment with MN-PLGA extract, MN-MgH_2 extract, MgH_2 solution or normal cell culture medium (control group). e) RT-qPCR for IL-6, IL-1β, iNOS, Arg-1 after 24-h treatment with MN-MgH_2 extract or normal cell culture medium (control group). n = 4, *p < 0.05, **p < 0.01, ***p < 0.001, ****p < 0.0001.

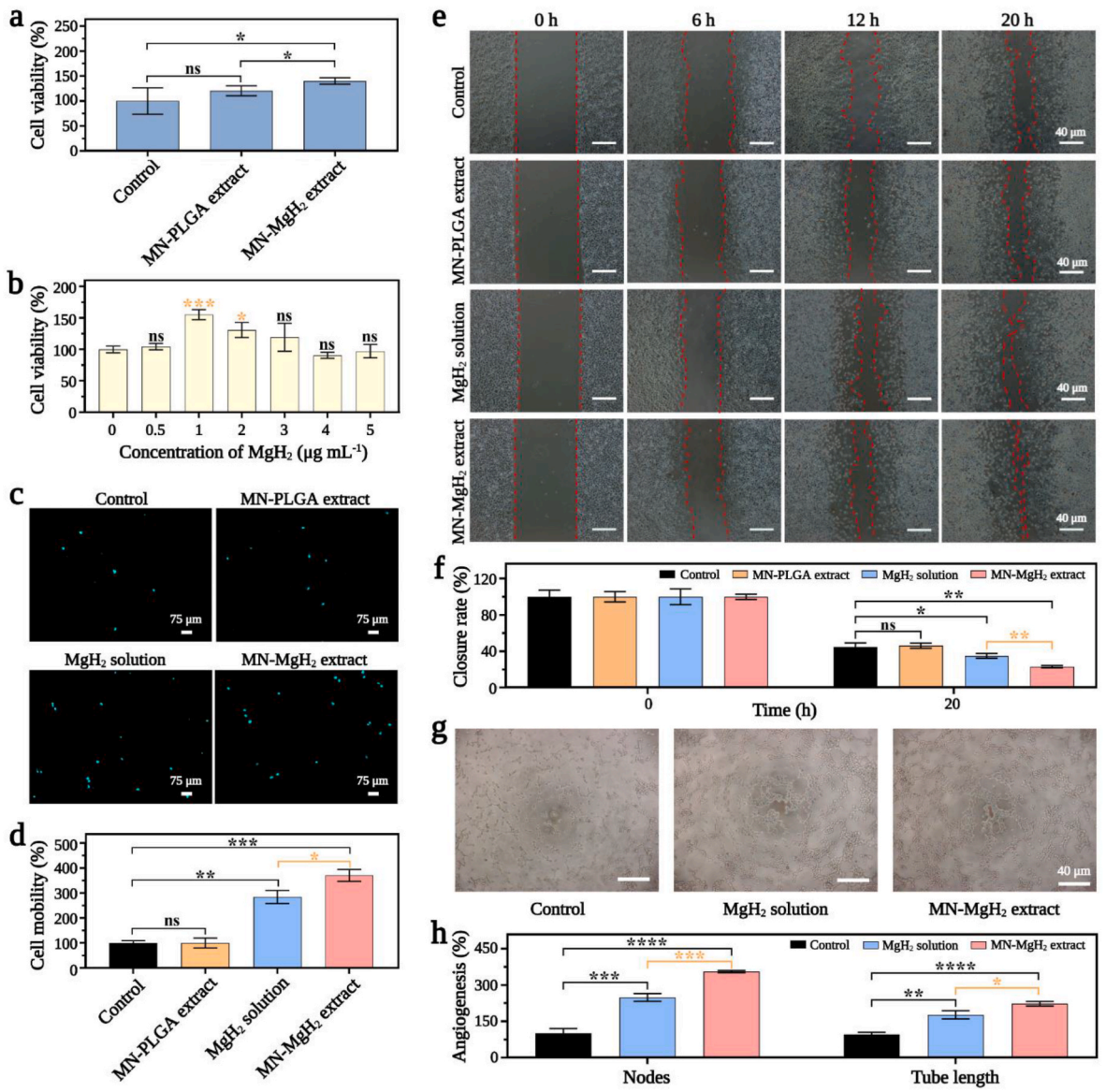

Fig. 4. *In vitro* cytotoxicity, cell regeneration and angiogenesis effects of MN-MgH_2. a) Cell viability of fibroblasts after 72-h treatment with MN-PLGA extract, MN-MgH_2 extract or normal cell culture medium (control group). b) Cell viability of fibroblasts after treated with varied concentrations of MgH_2 for 72 h. c) Confocal images of migrated HUVECs in Transwell experiment after 24-h treatment with MN-PLGA extract, MN-MgH_2 extract, MgH_2 solution or normal cell culture medium (control group). Nucleus was stained with Hoechst (cyan). d) Quantification result of migration rate of HUVECs in Transwell experiment after different treatments for 24 h, which is corresponding to the images presented in (c). e) Fibroblasts migration evaluated using cell migration assay after different treatments for 24 h. f) Quantification of the gap closure ratio in each group, which is corresponding to the images presented in (e). g) Images of HUVECs after 4-h treatment with MN-MgH_2 extract, MgH_2 solution or normal cell culture medium (control group). h) Quantifications of nodes and tube length in each group. n = 3, *p < 0.05, **p < 0.01, ***p < 0.001, ****p < 0.0001.

1.95-fold, respectively (Fig. 6b). It is worth noting that the ROS reduction induced by MN-MgH_2 was 1.18 times more significant than that by MgH_2 powder. Normally, days 1–5 post-injury is the inflammatory phase [36] when the extensive ROS accumulate in the wound area [37]. Hence, the control group showed a slight decrease on ROS reduction on day 7. Yet, the ROS production after the treatments of MgH_2 powder and MN-MgH_2 was still statistically decreased by 1.32-fold and 1.64-fold, respectively, on day 7. Meanwhile, there was still a statistically significant difference between MgH_2 powder and MN-MgH_2 group (Fig. 6b). In conclusion, the treatment of MN-MgH_2 significantly decreased the production of ROS *in vivo* and therefore promoted the wound healing.

2.7. MN-MgH_2 induced M2 repolarization in vivo

To verify the function of MN-MgH_2 in M2 repolarization, *in vivo* immunofluorescence staining of pan macrophage marker (CD68, in red), M1 macrophages marker (iNOS, in green) and M2 macrophages marker (CD206, in green) was performed on wound tissues from different groups. Normally, the M1 macrophages would be the predominant macrophage phenotype from day 1 to day 3, while the M2 macrophages usually peak on day 7 after injury. On day 3, the representative images of CD68/iNOS double-staining (Fig. 7a) and the quantification of $CD68^+iNOS^+$ cells number (Fig. 7b) indicate that MgH_2 powder and MN-MgH_2 treatment decreased M1 polarization by 3.08-fold and 6.69-fold, respectively, compared to the control group. On day 7, the MN-MgH_2 group continued to show a statistical decrease on M1 macrophages by 7.60-fold, while the MgH_2 powder group only decrease it by 3.00-fold, compared to the control group (Fig. 7b). Furthermore, the MN-MgH_2 still lowered the M1 polarization by 7.06-fold on day 14, while the MgH_2 powder group only decrease it by 1.67-fold (Fig. 7b).

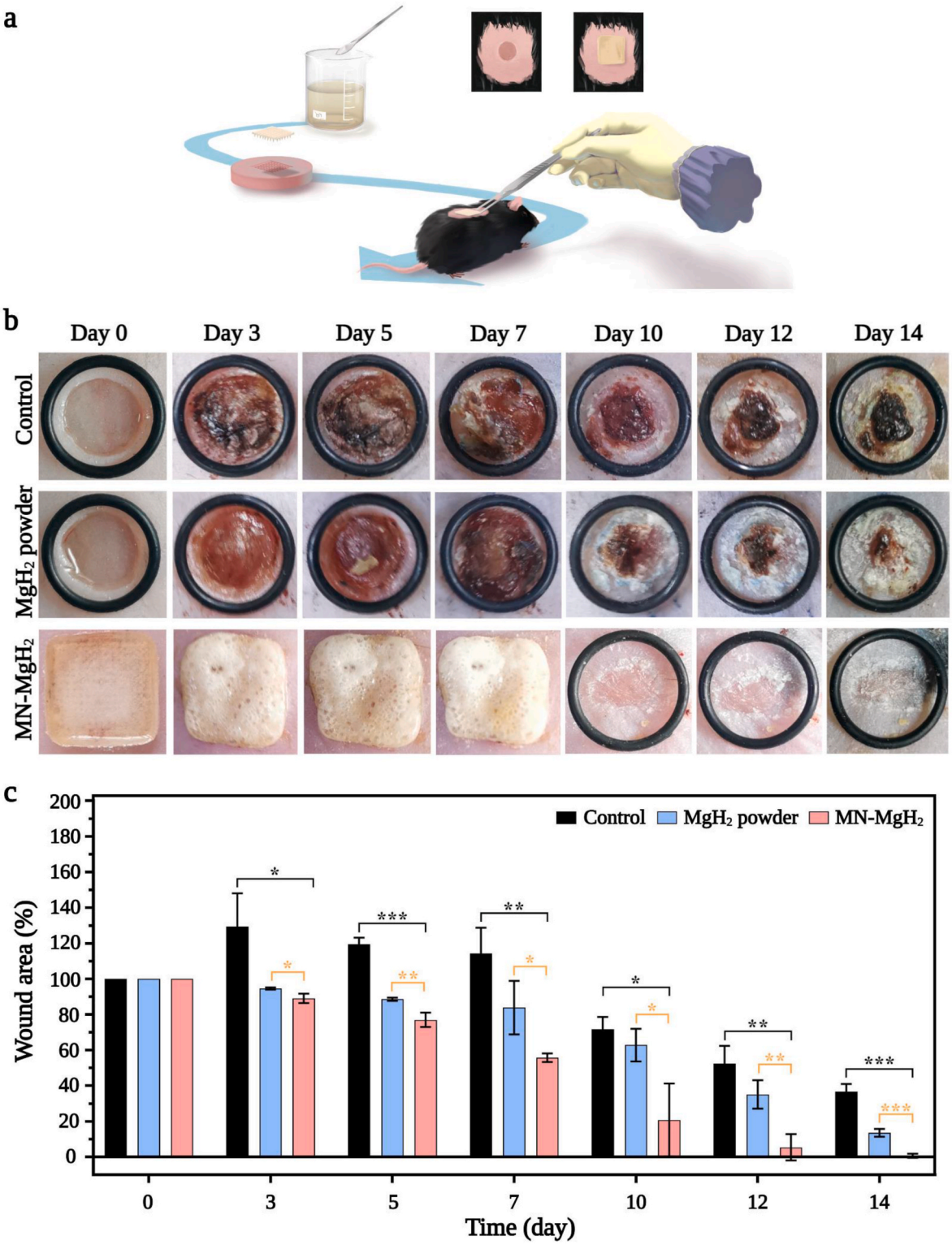

Fig. 5. *In vivo* wound healing evaluation with diabetic mice. a) Schematic illustration of intelligent microneedle patch treatment *in vivo*. b) Representative photographic images of the diabetic wounds with different treatments after 0, 3, 5, 7, 10, 12 and 14 days, respectively. MN-MgH_2 was not removed until it came off naturally on day 10. c) Quantification of wounded area healing rate in each group. n = 3, *p < 0.05, **p < 0.01, ***p < 0.001, ****p < 0.0001.

Overall, we have demonstrated that MN-MgH_2 led to more significant reduction in M1 macrophages *in vivo*, compared to the control and MgH_2 powder groups. Next, the analysis of CD68/CD206 double-staining was applied to investigate the M2 repolarization. The results indicated that the treatment of MgH_2 powder and MN-MgH_2 increased the M2 repolarization by 2.04-fold and 2.31-fold, respectively, on day 3 (Fig. 8a, **b)**, compared to the control group. On day 7, MgH_2 powder and MN-MgH_2 groups increased M2 repolarization by 1.71-fold and 1.93-fold, respectively (Fig. 8b). On day 14, the treatment of MgH_2 powder and MN-MgH_2 consistently enhanced the repolarization by 1.32-fold and 1.54-fold (Fig. 8b). Compared with MgH_2 powder group, MN-MgH_2 group increased M2 repolarization by 1.12-fold and 1.15-fold on day 7 and day

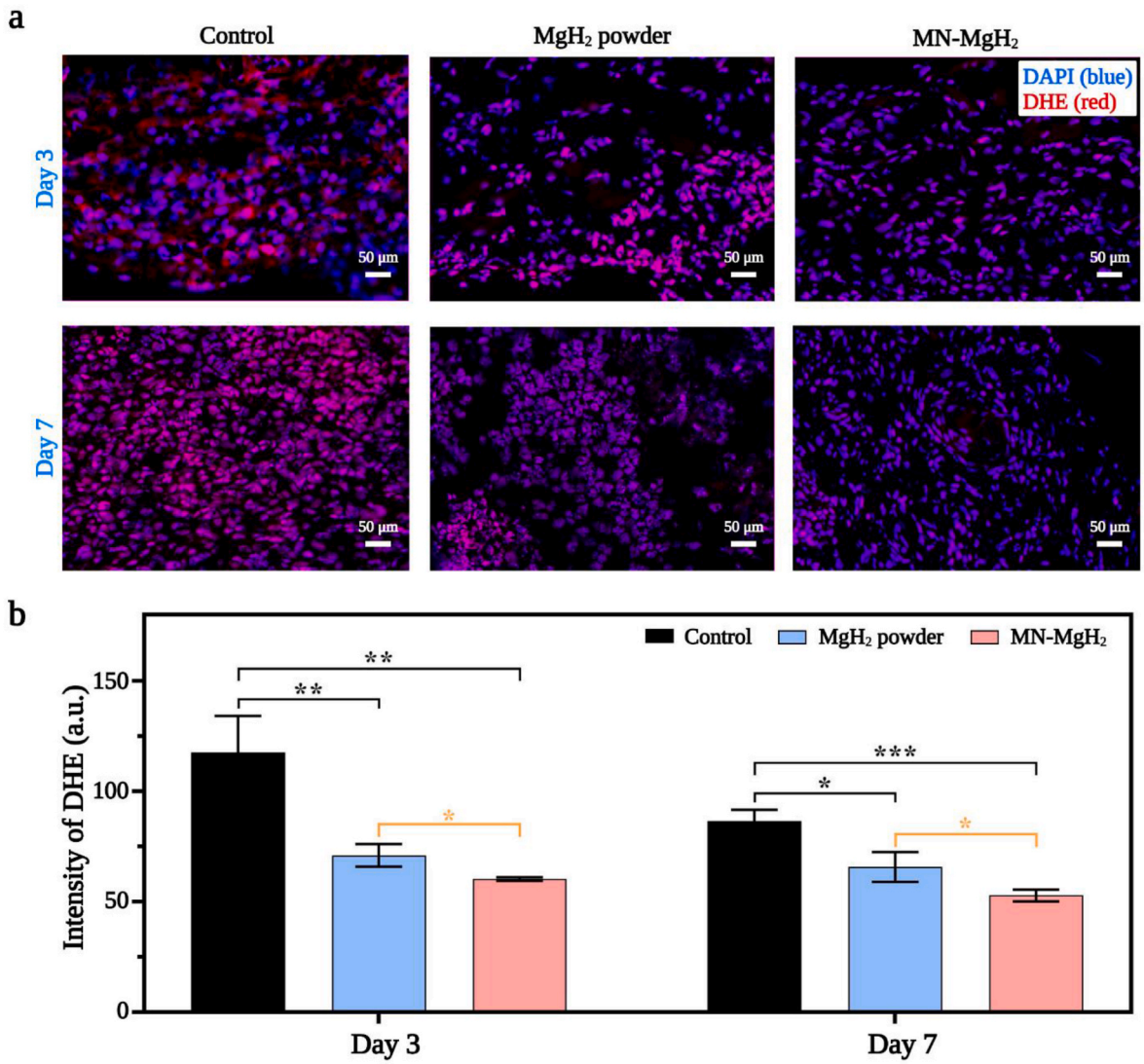

Fig. 6. *In vivo* ROS reduction induced by MN-MgH_2. a) Representative images of ROS staining of the wound tissues in control, MgH_2 powder and MN-MgH_2 groups on day 3 and day 7, respectively. Nucleus was stained with DAPI (blue), and ROS was stained with DHE (red). b) Fluorescence intensity quantification of DHE in each group on day 3 and 7, respectively. n = 3, *p < 0.05, **p < 0.01, ***p < 0.001, ****p < 0.0001.

14, indicating the enhanced Mg^{2+} release from MN-MgH_2.

Although, theoretically, both MgH_2 powder and MN-MgH_2 can generate $Mg(OH)_2$ and release Mg^{2+} to promote the repolarization of M2, the dissolved PLGA and its acidic degradation products in MN-MgH_2 group would neutralize the alkaline and constantly promoted the Mg^{2+} releasing. Therefore, MN-MgH_2 demonstrated significantly decreased M1 polarization and increased M2 repolarization on day 3, day 7 and day 14, compared to the treatment of MgH_2 powder. In conclusion, it has been demonstrated that the applications of MN-MgH_2 reduced M1 polarization and promoted M2 repolarization *in vivo*.

2.8. MN-MgH_2 promoted tissue regeneration, collagen fibre repair and angiogenesis in vivo

H&E staining was used for observing granulation tissue formation and measuring organization level, in order to investigate the epithelial formation process (Fig. 9a, first column). The results show that the epithelial tissue in the MN-MgH_2 group was completely formed after 10 days of treatment. In comparison, epithelial tissues in the control group and MgH_2 powder group still had several fat cavities which were circled with orange lines, reflecting the incomplete healing. Furthermore, Masson's trichrome staining was used to detect and distinguish collagen fibres from muscle fibres in animal tissues by staining collagen fibres into blue (or green), muscle fibre into red, and cell nuclei into blue (Fig. 9a, second column). Tissues in the MN-MgH_2 group obtained the best collagen deposition and oriented arrangement, indicating better wound healing and tissue remodeling outcomes.

Moving forward, anti-CD31 (Fig. 9b) and anti-Ki67 (Fig. 9c) immunofluorescence stainings were utilized to assess cell proliferation and capillary formation *in vivo* after different treatments. The staining region of CD31 and Ki67 in the skin tissue was indicated in Fig. S7. Quantified capillary density (in dermis) in each group by counting the number of regenerative capillaries is shown in Fig. 9d, which suggests that the treatment of MN-MgH_2 resulted in a 2.48-fold increase in the capillarity compared with the control group and it was 1.48 times more than that of the MgH_2 powder group. The proliferated cells in the epidermis layer and dermis layer were also quantified separately. Although both MgH_2 powder and MN-MgH_2 treatments promoted the proliferation of cells in the epidermis (Fig. 9e), the treatment of MN-MgH_2 led to a 5.2 times more significant proliferation than that of control group in the dermis layer and particularly, it was 1.5 times more than that of the MgH_2 powder group (Fig. 9f). In conclusion, capillary formation and cell proliferation of the control group and MgH_2 powder group were mainly observed on the surface of tissues, while the MN-MgH_2 group achieved

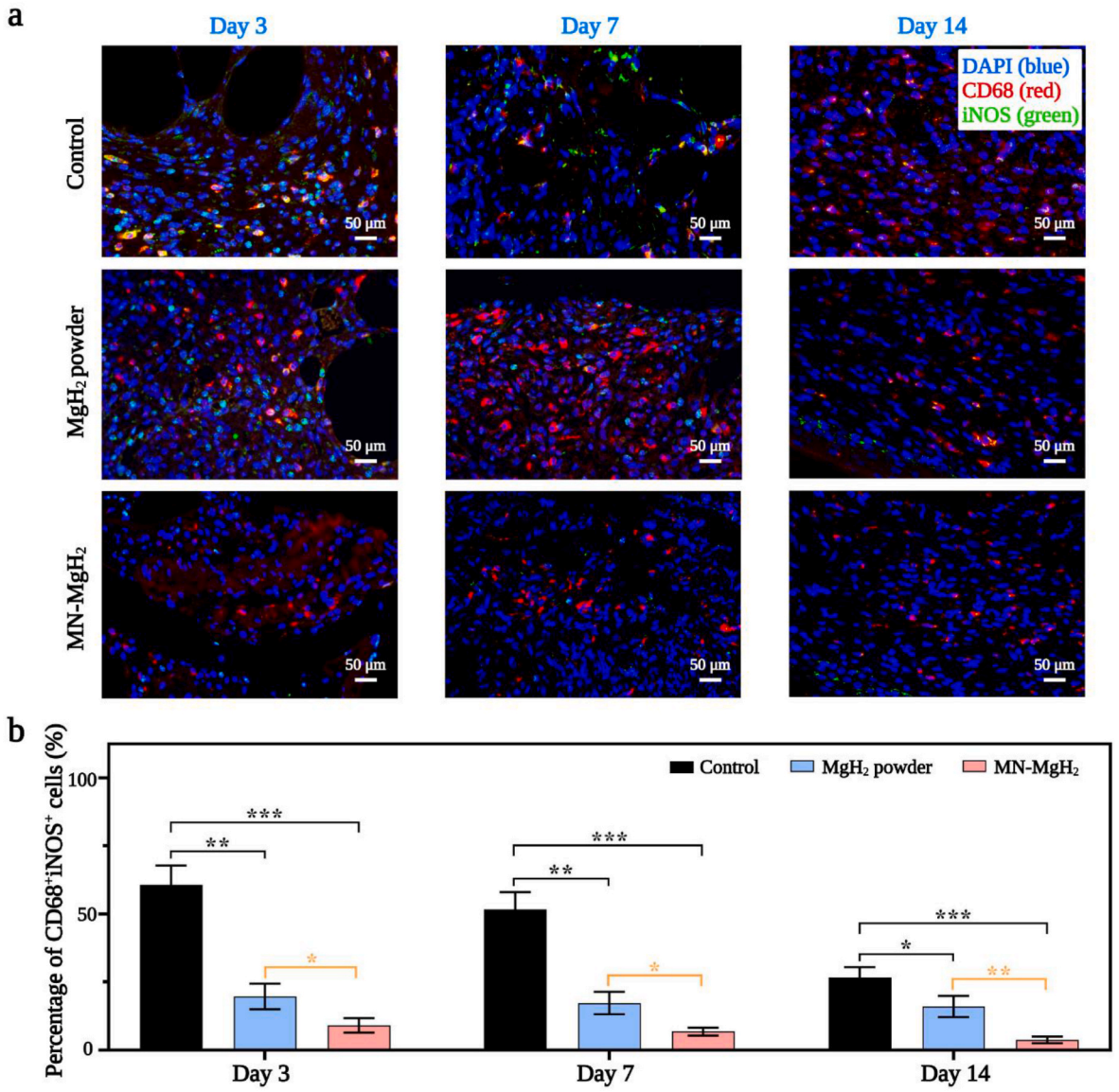

Fig. 7. Immunofluorescence staining for M1 polarization. Pan macrophage was stained with CD68 (red), M1 macrophage was stained with iNOS (green), and nucleus was stained with DAPI (blue). a) Representative images of CD68 and iNOS double staining of the wound tissues in the control, MgH_2 powder and MN-MgH_2 groups after 3, 7 and 14 days of treatment, respectively. b) Quantification of the percentage of $CD68^+iNOS^+$ cells in each group after 3, 7 and 14 days of treatment, respectively. n = 3, *p < 0.05, **p < 0.01, ***p < 0.001, ****p < 0.0001.

more regenerative capillaries and cells in the dermal tissue layer due to the merit of microneedle delivery.

3. Conclusion

In summary, MN-MgH_2 combined the therapeutic effects of Mg^{2+} and H_2 and functioned in the deep layer of tissues for wound healing. The introduction of a multifunctional MN-MgH_2 optimized therapeutic efficacy by i) sustainable and accelerated release of $Mg^{2+}$and H_2; ii) ROS reduction enabled by H_2 therapy; iii) enhanced polarization of M2 macrophages phenotype enabled by Mg^{2+}. The multiple functions of MN-MgH_2 were systematically investigated both in vitro and *in vivo*, and proved to be effective in anti-inflammatory, cell proliferation and migration, angiogenesis and tissue regeneration. This MN-MgH_2 that integrated various therapeutic functions provides a novel approach for improving diabetic wound healing.

4. Materials and methods

4.1. Materials and cell culture

PLGA was purchased from Sigma-Aldrich. MgH_2 was fractured by Center of Hydrogen Science, Shanghai Jiao Tong University. Microneedle patch molds were made up of polydimethylsiloxane (PDMS) purchased from Micropoint Technologies Pte. Ltd. (Singapore). Every microneedle patch had a 10 × 10 array, the size of which was 200 μm × 200 μm × 500 μm (W × L × H). High-glucose DMEM cell culture medium and Fetal Bovine Serum (FBS) were purchased from Gibco (UK). Cell lines including fibroblasts, HUVECs and Raw264.7 cells were cultured with a complete medium (high-glucose DMEM cell culture medium with 10% FBS) in an incubator (37 °C, 5% CO_2).

4.2. Fabrications of PLGA, MN-PLGA and MN-MgH_2

10 wt% PLGA solution was used, which was formed by dissolving 100 mg PLGA in 1 mL 1, 4-dioxane and stirring for 30 min [38]. 10 mg

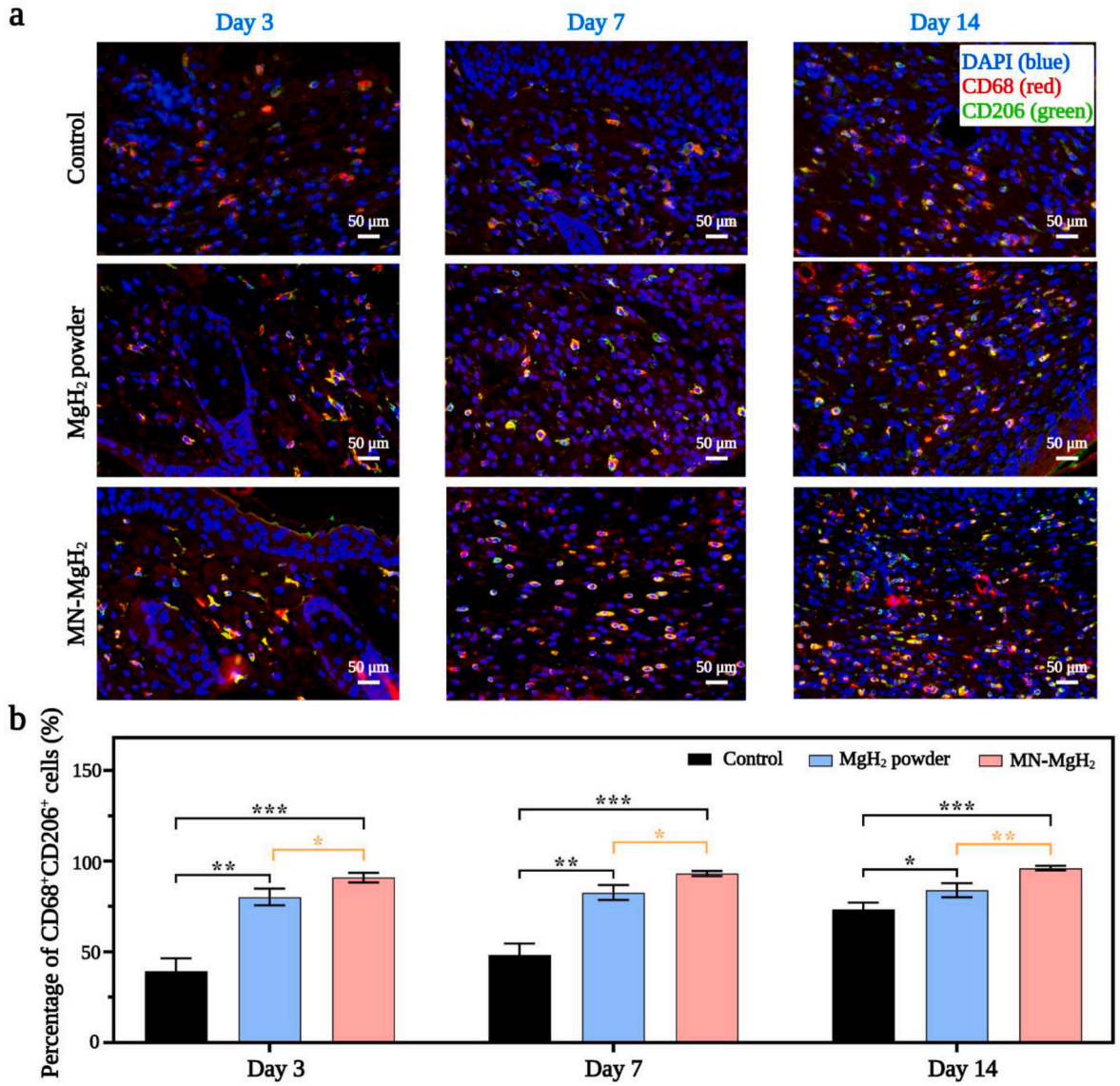

Fig. 8. Immunofluorescence staining for M2 polarization. Pan macrophage was stained with CD68 (red), M2 macrophage was stained with CD206 (green), and nucleus was stained with DAPI (blue). a) Representative images of CD68 and CD206 double staining of the wound tissues in the control, MgH_2 powder and MN-MgH_2 groups after 3, 7 and 14 days of treatment, respectively. b) Quantification of the percentage of $CD68^+CD206^+$ cells in each group after 3, 7 and 14 days of treatment, respectively. n = 3, *p < 0.05, **p < 0.01, ***p < 0.001, ****p < 0.0001.

MgH_2 was added and uniformly distributed into the PLGA solution to achieve a PLGA-MgH_2 solution. The PLGA-MgH_2 solution was then added to the microneedle models and centrifuged at 3000 rpm for 5 min to ensure that the solution fully filled the tips of the microneedle model. Every microneedle model contained a 300 μL PLGA-MgH_2 solution which was then placed into a dryer for 40 °C. After 12 h, the microneedle rigidified and was demolded to get the MN-MgH_2. MN-PLGA was made by using the same fabrication procedure.

4.3. *In vitro release profiles of Mg^{2+} and H_2 from MgH_2 powder and MN-MgH_2*

To test the release profile of H_2 from MgH_2 powder and MN-MgH_2 in vitro, 3 mg MgH_2 powder or one patch of MN-MgH_2 was placed and immediately sealed in a penicillin bottle (the volume was 15 mL) containing 10 mL pure water (pH = 7.0). 1 mL gas was taken at different time points (0 h, 5 min, 10 min, 30 min, 1 h, 3 h, 6 h, 12 h, 1 day, 2 days, 3 days, 5 days and 7 days) and the amount of H_2 was measured by a gas chromatograph (Agilent 7890 B, USA).

The release profiles of Mg^{2+} from MgH_2 powder and MN-MgH_2 were also tested in pure water (pH = 7.0). 30 mg MgH_2 powder or ten patches of MN-MgH_2 were immersed in 10 mL pure water, and placed in a dialysis bag. The bag was then placed in a beaker with 100 mL pure water. ICP-OES testing (Optima 7000DV, Perkin Elmer, USA) was taken at different time points (0 h, 5 min, 10 min, 30 min, 1 h, 3 h, 6 h, 12 h, 1 day, 2 days, 3 days, 5 days and 7 days) to quantify the amount of Mg^{2+}.

The changes of pH value were tested in pure water. 3 mg MgH_2 powder, one patch of MN-PLGA or one patch of MN-MgH_2 was immersed in 15 mL pure water (pH = 7.0) and the pH values of different groups were measured at different time points (0 h, 5 min, 10 min, 30 min, 1 h, 3 h, 6 h, 12 h, 1 day, 2 days, 3 days, 5 days and 7 days).

The release profile of H_2 from MgH_2 at different pH values was tested via placing 3 mg MgH_2 powder in 10 mL pure water with different pH values (pH = 2, 3, 4, 5, 6, 7) for 3 days. Then, 1 mL gas was taken and the amount of H_2 was measured by a gas chromatograph (Agilent 7890 B, USA).

The formation of the $Mg(OH)_2$ layer on MgH_2 particles was also characterized with SEM and elemental imaging. After immersing in the

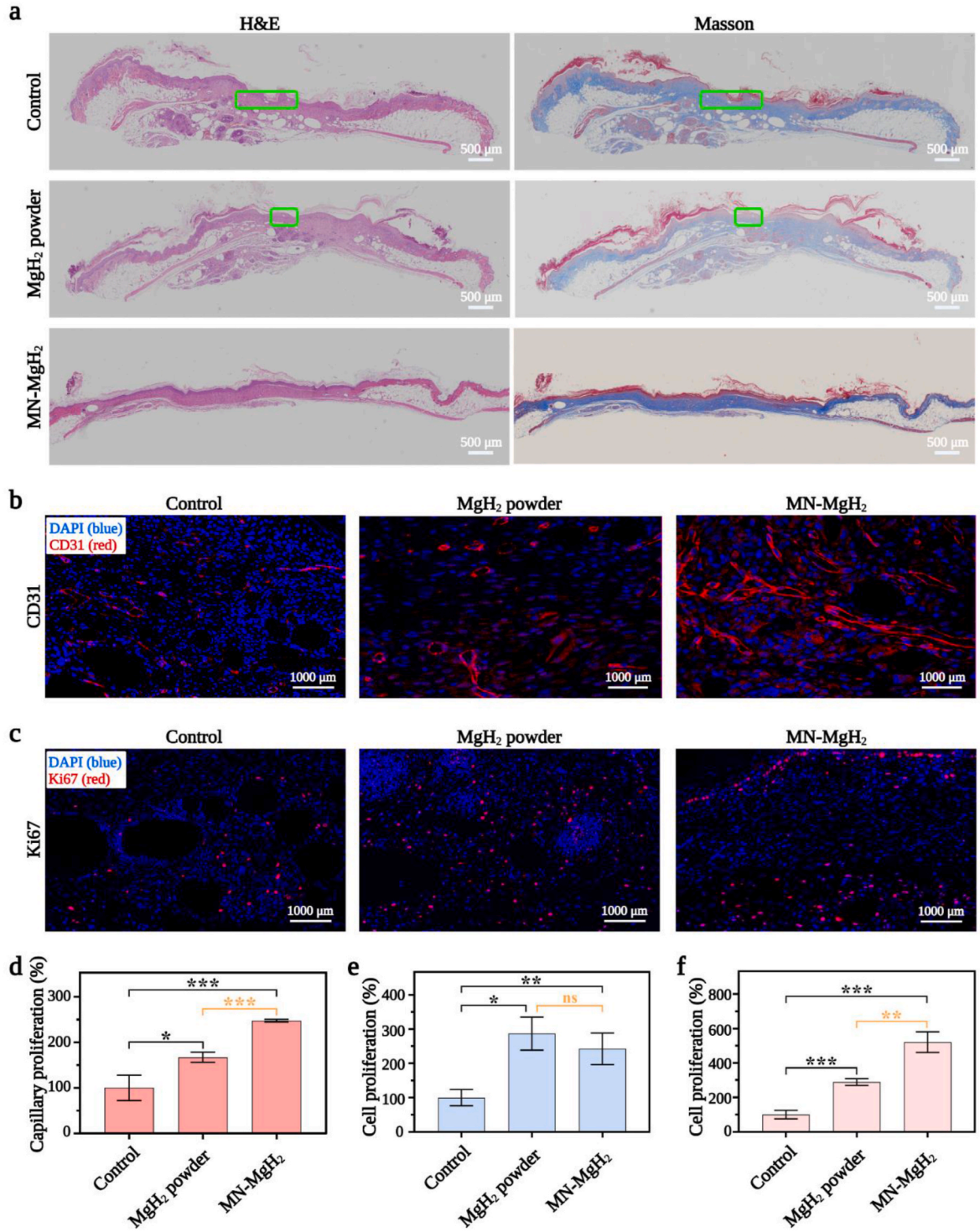

Fig. 9. *In vivo* investigation on the tissue regeneration, collagen fibrils repair, cell proliferation and angiogenesis efficacy of MN-MgH_2. a) H&E and Masson's trichrome staining of wound tissues in control, MgH_2 powder and MN-MgH_2 groups after 14 days of treatment. Green lines indicate fat cavitation. b) Representative images of anti-CD31 (red) immunofluorescence staining of dermis layer in wound area in control, MgH_2 powder and MN-MgH_2 groups after 14 days of treatment. Nucleus was stained with DAPI (blue). c) Representative images of anti-Ki67 (red) and immunofluorescence staining of dermis layer in wound area in control, MgH_2 powder and MN-MgH_2 groups after 14 days of treatment. Nucleus was stained with DAPI (blue). d) Quantification of the capillary density of dermis layer in wound area in each group. e) Quantification of the cell proliferation rate of wound tissues in the epidermis in each group. f) Quantification of cell proliferation rate of wound tissues in the dermis in each group. n = 3, *p < 0.05, **p < 0.01, ***p < 0.001, ****p < 0.0001.

pure water (pH = 7.0) for 7 days, one patch of MN-MgH_2 was removed from the bottle and dissolved in 1,4-dioxane to collect the post-reaction MgH_2 powder, which was then photographed with High Resolution Scanning Electron Microscope (APREO S, Thermo scientific). Afterwards, the distribution of Mg and O was tested with an Energy Dispersive Spectrometer. MgH_2 powder treated with pure water (pH = 7.0) for 7 days or without any treatment was also tested using the same procedure.

4.4. CCK-8 assay

Every patch of MN-PLGA or MN-MgH_2 was immersed in 5 mL PBS for 3 days to get the extracts. Fibroblasts were seeded into 96-well plates at 3000 cells per well and divided into 3 groups, namely the control group, MN-PLGA extract group and MN-MgH_2 extract group. After fibroblasts were cultured with 100 μL high-glucose DMEM for 12 h, they were cocultured with 90 μL complete medium mixed with 10 μL PBS or 10 μL extract of MN-PLGA or MN-MgH_2 for 3 days. On the third day, a complete medium with 10% of CCK-8 solution was added into every well to interact with living cells. After being placed in an incubator for 2 h, 96-well plates were analyzed with a microplate reader (SpectraMAX iD3, Molecular Devices. LLC., USA). For the concentration dependence experiment, Fibroblasts were cultured with high-glucose DMEM for 12 h, and then cocultured with different concentrations of MgH_2 solution (dissolved in complete medium) (0, 0.5, 1, 2, 3, 4, 5 μg mL^{-1}) for 3 days. Then, the cell viability was tested by using the CCK-8 assay following the same technical progress above.

4.5. Living/dead cell double staining

HUVECs were divided into 3 groups and seeded in confocal dishes with 40×10^4 cells per dish. Cells in different groups was either cocultured with one patch of MN-PLGA, MN-MgH_2 or cultured with only normal cell culture medium (control group) for 1 or 3 days. At the appointed time, the culture medium was removed and 300 μL Calcein-AM/PI assay which was fractured according to the manufacturer's protocol was added into every dish. After being incubated for 15 min (37 °C, 5% CO_2), cells in different groups were photographed with a confocal microscope (Leica SP5, Leica Camera AG, Germany) to record the representative images.

4.6. Tube formation analysis

First, every 50 μL Materigel was placed into one well of a 96-well plate according to the manufacturer's protocol. Then, HUVECs were isolated into DMEM and placed in 96-well plate with a density of 2×10^4 per well. Afterwards, HUVECs were divided into 3 groups and incubated with either normal cell culture medium (control group), MgH_2 solution (1 μg mL^{-1}) or MN-MgH_2 extract for 4 h, and then the representative images of each group were taken.

4.7. In vitro migration and wound healing analysis

750 μL complete medium was placed in every well of 24-well plates. Every 2×10^4 HUVECs were suspended in 200 μL high-glucose DMEM and seeded in one well of 24-well Transwell plates (Corning Incorporated, USA). Wells of 24-well Transwell plates have different processing factors according to different groups including interacting either with 100 μL extract of MN-PLGA, MN-MgH_2, MgH_2 solution (1 μg mL^{-1}), or normal cell culture medium. After interacting for 24 h, cells were first fixed with paraformaldehyde for 15 min, then stained with Hoechst (Beyotime, China) according to the manufacturer's protocol. Cells inside Transwells were wiped up, and the remained migratory cells were recorded with a confocal microscope (Leica SP5, Leica Camera AG, Germany). Fibroblasts were divided into 4 groups, after obtaining scratches with spreadheads in the middle of wells, cocultured with MN-PLGA extract, MN-MgH_2 extract, MgH_2 solution (1 μg mL^{-1}), or normal cell culture medium. The pattern of cell migration was recorded with an optical microscope after being cocultured for 0, 6, 12 and 20 h.

4.8. In vitro macrophage polarization analysis

For SEM analysis, 5×10^4 Raw264.7 cells were seeded into one well of a 24-well plate which contained a piece of sterilized silicon slice. After cocultured with MN-PLGA extract, MN-MgH_2 extract, MgH_2 solution (1 μg mL^{-1}) or normal cell culture medium for 24 h, silicon slices with Raw264.7 cells were removed from plates and fixed with 2.5% glutaraldehyde for 30 min and dehydrated in an alcohol concentration gradient (30% for 5 min, 50% for 5 min, 70% for 10 min, 80% for 10 min, 95% for 15 min, 100% for 15 min). Each group was photographed with SEM (Nikon ECLIPSE E 100, Nikon Corporation, Japan) afterwards. For RT-qPCR analysis, Raw264.7 cells were divided and cocultured with MN-MgH_2 extract or normal cell culture medium as above for 24 h. Afterwards, the RNA was entirely isolated and the RNA expression of IL-6, IL-1β, iNOS and Arg-1 were quantified while using GAPDH as a housekeeping gene.

4.9. In vitro flow analysis of ROS production

For flow analysis, Raw264.7 cells were first seeded in 6-well plates that contained 2 μg LPS (purchased from Sigma-Aldrich), then divided into 4 groups to cocultured with either 1 mL extract of MN-PLGA, MN-MgH_2 and MgH_2 solution (1 μg mL^{-1}) or normal cell culture medium (2 mL normal cell culture medium, control group). After 24 h cocultivation, Raw264.7 cells were stained with ROS assay kit (Beyotime, China) based on the manufacturer's protocol. Stained cells were first photographed with a fluorescence microscope, then collected and analyzed with flow cytometry (Beckman Coulter, US).

4.10. In vivo establishment of diabetic wound model and wound healing efficacy test of MgH_2 powder and MN-MgH_2

Diabetic (db/db) mice (8-week-old) (Nanjing University-Nanjing Biomedical Institute, China) were used for establishing a chronic wound model. A circle wound with a diameter being 6 mm was created on the back of every mouse after the mouse was anesthetized and shaved. Afterwards, 39 mice were randomly grouped to undertake different treatments (control group, MN-MgH_2 group and MgH_2 powder group). The control group had no treatment while mice in MN-MgH_2 group was treated with one patch of MN-MgH_2 which was not removed until it came off naturally and mice in MgH_2 powder group were treated with 3 mg MgH_2 powder. Mice were reared in separate cages with sufficient food and water. Images of wound areas were taken at 0, 3, 5, 7, 10, 12 and 14 days after treatment.

4.11. In vivo wound healing, ROS reduction and macrophage polarization analysis

After 3, 7 and 14 days of treatments, mice were sacrificed with an overdose of 4% chloraldrate. The skin tissues of the wound area were first removed and immersed in 4% paraformaldehyde for 24 h. After being embedded in wax blocks, samples were sliced with 5 μm thickness for the following staining. For testing the wounding healing process, hematoxylin and eosin (H&E), Masson trichrome staining and immunofluorescence staining using anti-CD31 (1:500) and anti-Ki67 (1:500) antibodies were applied. For testing the rate of ROS reduction in control group, MN-MgH_2 group and MgH_2 powder group, DHE were applied here. For testing the macrophage polarization, antibodies targeting CD68, CD206 and iNOS were utilized.

4.12. Statistical analysis

All data were collected in triplicate or quadruplicate and reported as mean and standard deviation. The comparison of two conditions was evaluated by the unpaired *t*-test. Except for the data of wound areas, angiogenesis and immunofluorescent intensity were analyzed with Image J, all data was evaluated with GraphPad. *$p < 0.05$, **$p < 0.01$, ***$p < 0.001$, ****$p < 0.0001$ were considered statistically significant differences, and ns indicates no significant difference.

Data availability

The authors declare that the main data supporting the findings of this study are available within the article and its Supplementary Information. Extra data are available from the corresponding author upon request.

Ethics approval and consent to participate

All experimental procedures were conducted in accordance with institutional guidelines for the care and use of laboratory animals and protocols, which were approved by the Animal Care and Use Committee of Shanghai Ninth People's Hospital.

Declaration of competing interest

The authors declare no conflict of interest.

CRediT authorship contribution statement

Pei Wang: Conceptualization, Methodology, Investigation, Writing – original draft. **Jiayingzi Wu:** Methodology, Formal analysis, Writing – original draft, Funding acquisition. **Haiyan Yang:** Methodology, Formal analysis. **Hengke Liu:** Methodology, Formal analysis. **Tianyu Yao:** Methodology, Formal analysis. **Chang Liu:** Methodology, Formal analysis. **Yan Gong:** Methodology, Formal analysis. **Mingsong Wang:** Methodology, Formal analysis. **Guangyu Ji:** Methodology, Formal analysis. **Peng Huang:** Conceptualization, Supervision, Funding acquisition. **Xiansong Wang:** Conceptualization, Supervision, Funding acquisition.

Acknowledgements

This work was financially supported by the National Natural Science Foundation of China (31971271, 22104094), National Key R&D Program of China (2020YFA0908800, 2018YFA0704000), Basic Research Program of Shenzhen (JCYJ20200109105620482, JCYJ20180507182413022), Shenzhen Science and Technology Program (KQTD20190929172538530) and supported by the Funding from Center of Hydrogen Science, Shanghai Jiao Tong University, China. All experimental procedures were conducted in accordance with institutional guidelines for the care and use of laboratory animals and protocols, which were approved by the Animal Care and Use Committee of Shanghai Ninth People's Hospital. We would like to thank the Instrumental Analysis Center of SJTU for the SEM, FTIR, and TGA analyses.

Appendix A. Supplementary data

Supplementary data to this article can be found online at https://doi.org/10.1016/j.bioactmat.2023.01.001.

References

[1] S. Bellary, I. Kyrou, J.E. Brown, C.J. Bailey, Type 2 diabetes mellitus in older adults: clinical considerations and management, Nat. Rev. Endocrinol. 17 (2021) 534–548.
[2] Y. Zheng, S.H. Ley, F.B. Hu, Global aetiology and epidemiology of type 2 diabetes mellitus and its complications, Nat. Rev. Endocrinol. 14 (2018) 88–98.
[3] A. American Diabetes, Classification and diagnosis of diabetes: standards of medical care in diabetes-2021, 2. Diabetes Care 44 (2021) S15–S33.
[4] S. Khosla, P. Samakkarnthai, D.G. Monroe, J.N. Farr, Update on the pathogenesis and treatment of skeletal fragility in type 2 diabetes mellitus, Nat. Rev. Endocrinol. 17 (2021) 685–697.
[5] O.C. Rabe, M. Winther-Jensen, K.H. Allin, O.L. Svendsen, Fractures and osteoporosis in patients with diabetes with charcot foot, Diabetes Care 44 (2021) 2033–2038.
[6] N. Singh, D.G. Armstrong, B.A. Lipsky, Preventing foot ulcers in patients with diabetes, JAMA 293 (2005) 217–228.
[7] A.E. Louiselle, S.M. Niemiec, C. Zgheib, K.W. Liechty, Macrophage polarization and diabetic wound healing, Transl. Res. 236 (2021) 109–116.
[8] Y. Qian, Y. Zheng, J. Jin, X. Wu, K. Xu, M. Dai, Q. Niu, H. Zheng, X. He, J. Shen, Immunoregulation in diabetic wound repair with a photoenhanced glycyrrhizic acid hydrogel scaffold, Adv. Mater. (2022) 34.
[9] A. American Diabetes, 11. Microvascular complications and foot care: standards of medical care in diabetes-2021, Diabetes Care 44 (2021) S151–S167.
[10] S. Wilson, P. Mone, U. Kansakar, S.S. Jankauskas, K. Donkor, A. Adebayo, F. Varzideh, M. Eacobacci, J. Gambardella, A. Lombardi, G. Santulli, Diabetes and restenosis, Cardiovasc. Diabetol. 21 (2022) 23.
[11] A. Ceriello, F. Prattichizzo, Variability of risk factors and diabetes complications, Cardiovasc. Diabetol. 20 (2021) 101.
[12] F. Paneni, J.A. Beckman, M.A. Creager, F. Cosentino, Diabetes and vascular disease: pathophysiology, clinical consequences, and medical therapy: part I, Eur. Heart J. 34 (2013) 2436–2443.
[13] W. Ahmad, B. Ijaz, K. Shabbiri, F. Ahmed, S. Rehman, Oxidative toxicity in diabetes and Alzheimer's disease: mechanisms behind ROS/RNS generation, J. Biomed. Sci. 24 (2017) 76.
[14] S. Li, L. Zheng, J. Zhang, X. Liu, Z. Wu, Inhibition of ferroptosis by up-regulating Nrf2 delayed the progression of diabetic nephropathy, Free Radic. Biol. Med. 162 (2021) 435–449.
[15] X. Qi, Y. Xiang, E. Cai, S. You, T. Gao, Y. Lan, H. Deng, Z. Li, R. Hu, J. Shen, All-in-one: harnessing multifunctional injectable natural hydrogels for ordered therapy of bacteria-infected diabetic wounds, Chem. Eng. J. 439 (2022), 135691.
[16] L.A. Leiter, D.L. Bhatt, D.K. McGuire, H. Teoh, K. Fox, T. Simon, S.R. Mehta, E. I. Lev, R.G. Kiss, A.J. Dalby, H. Bueno, W. Ridderstråle, A. Himmelmann, J. Prats, Y. Liu, J.J. Lee, J. Amerena, M.N. Kosiborod, P.G. Steg, Diabetes-related factors and the effects of ticagrelor plus aspirin in the THEMIS and THEMIS-PCI Trials, J. Am. Coll. Cardiol. 77 (2021) 2366–2377.
[17] G.E. Umpierrez, D.C. Klonoff, Diabetes technology update: use of insulin pumps and continuous glucose monitoring in the hospital, Diabetes Care 41 (2018) 1579–1589.
[18] I. Ohsawa, M. Ishikawa, K. Takahashi, M. Watanabe, K. Nishimaki, K. Yamagata, K. Katsura, Y. Katayama, S. Asoh, S. Ohta, Hydrogen acts as a therapeutic antioxidant by selectively reducing cytotoxic oxygen radicals, Nat. Med. 13 (2007) 688–694.
[19] M.Y. Liu, F. Xie, Y. Zhang, T.T. Wang, S.N. Ma, P.X. Zhao, X. Zhang, T.W. Lebaron, X.L. Yan, X.M. Ma, Molecular hydrogen suppresses glioblastoma growth via inducing the glioma stem-like cell differentiation, Stem Cell Res. Ther. 10 (2019) 145.
[20] G. Zhou, E. Goshi, Q. He, Micro/Nanomaterials-augmented hydrogen therapy, Adv. Healthc. Mater. 8 (2019), e1900463.
[21] L. Zhang, P. Zhao, C. Yue, Z. Jin, Q. Liu, X. Du, Q. He, Sustained release of bioactive hydrogen by Pd hydride nanoparticles overcomes Alzheimer's disease, Biomaterials 197 (2019) 393–404.
[22] P. Zhao, Z. Jin, Q. Chen, T. Yang, D. Chen, J. Meng, X. Lu, Z. Gu, Q. He, Local generation of hydrogen for enhanced photothermal therapy, Nat. Commun. 9 (2018).
[23] B. Zhao, Y. Wang, X. Yao, D. Chen, M. Fan, Z. Jin, Q. He, Photocatalysis-mediated drug-free sustainable cancer therapy using nanocatalyst, Nat. Commun. (2021) 12.
[24] T. Yang, Z. Jin, Z. Wang, P. Zhao, B. Zhao, M. Fan, L. Chen, T. Wang, B.-L. Su, Q. He, Intratumoral high-payload delivery and acid-responsive release of H2 for efficient cancer therapy using the ammonia borane-loaded mesoporous silica nanomedicine, Appl. Mater. 11 (2018) 136–143.
[25] Z. Jin, Y. Sun, T. Yang, L. Tan, P. Lv, Q. Xu, G. Tao, S. Qin, X. Lu, Q. He, Nanocapsule-mediated sustained H_2 release in the gut ameliorates metabolic dysfunction-associated fatty liver disease, Biomaterials 276 (2021), 121030.
[26] L. Liu, Y. Wu, J. Ye, Q. Fu, L. Su, Z. Wu, J. Feng, Z. Chen, J. Song, Synthesis of magnesium nanoparticle for NIR-II-photoacoustic-imaging-guided synergistic burst-like and H_2 cancer therapy, Chem 8 (2022) 1.
[27] W.L. Wan, Y.J. Lin, P.C. Shih, Y.R. Bow, Q. Cui, Y. Chang, W.T. Chia, H.W. Sung, An in situ depot for continuous evolution of gaseous H_2 mediated by a magnesium passivation/activation cycle for treating osteoarthritis, Angew. Chem., Int. Ed. Engl. 57 (2018) 9875–9879.
[28] F. Czerwinski, Controlling the ignition and flammability of magnesium for aerospace applications, Corrosion Sci. 86 (2014) 1–16.
[29] N. Yang, F. Gong, B. Liu, Y. Hao, Y. Chao, H. Lei, X. Yang, Y. Gong, X. Wang, Z. Liu, L. Cheng, Magnesium galvanic cells produce hydrogen and modulate the tumor microenvironment to inhibit cancer growth, Nat. Commun. 13 (2022) 2336.
[30] X. Shen, Y. Zhang, P. Ma, L. Sutrisno, Z. Luo, Y. Hu, Y. Yu, B. Tao, C. Li, K. Cai, Fabrication of magnesium/zinc-metal organic framework on titanium implants to inhibit bacterial infection and promote bone regeneration, Biomaterials 212 (2019) 1–16.
[31] Z. Zheng, Y. Chen, H. Hong, Y. Shen, Y. Wang, J. Sun, X. Wang, The "Yin and Yang" of immunomodulatory magnesium-enriched graphene oxide nanoscrolls decorated biomimetic scaffolds in promoting bone regeneration, Adv. Healthc. Mater. 10 (2021), 2000631.
[32] M. Bessa-Goncalves, A.M. Silva, J.P. Bras, H. Helmholz, B.J.C. Luthringer-Feyerabend, R. Willumeit-Romer, M.A. Barbosa, S.G. Santos, Fibrinogen and magnesium combination biomaterials modulate macrophage phenotype, NF-kB signaling and crosstalk with mesenchymal stem/stromal cells, Acta Biomater. 114 (2020) 471–484.
[33] L. Xu, R. Willumeit-Romer, B.J.C. Luthringer-Feyerabend, Effect of magnesium-degradation products and hypoxia on the angiogenesis of human umbilical vein endothelial cells, Acta Biomater. 98 (2019) 269–283.
[34] P. Wang, Y. Wang, Y. Yi, Y. Gong, H. Ji, Y. Gan, F. Xie, J. Fan, X. Wang, MXenes-integrated microneedle combined with asiaticoside to penetrate the cuticle for treatment of diabetic foot ulcer, J. Nanobiotechnol. 20 (2022) 259.

[35] M. Yin, J. Wu, M. Deng, P. Wang, G. Ji, M. Wang, C. Zhou, N.T. Blum, W. Zhang, H. Shi, N. Jia, X. Wang, P. Huang, Multifunctional magnesium organic framework-based microneedle patch for accelerating diabetic wound healing, ACS Nano 15 (2021), 17842.

[36] A.S. Kimball, F.M. Davis, A. denDekker, A.D. Joshi, M.A. Schaller, J. Bermick, X. Xing, C.F. Burant, A.T. Obi, D. Nysz, S. Robinson, R. Allen, N.W. Lukacs, P. K. Henke, J.E. Gudjonsson, B.B. Moore, S.L. Kunkel, K.A. Gallagher, The histone methyltransferase setdb2 modulates macrophage phenotype and uric acid production in diabetic wound repair, Immunity 51 (2019) 258–271 e255.

[37] H. Zhao, J. Huang, Y. Li, X. Lv, H. Zhou, H. Wang, Y. Xu, C. Wang, J. Wang, Z. Liu, ROS-scavenging hydrogel to promote healing of bacteria infected diabetic wounds, Biomaterials 258 (2020), 120286.

[38] X. Wang, A. Ai, Z. Yu, M. Deng, W. Liu, G. Zhou, W. Li, W. Zhang, Y. Cao, X. Wang, Dual-modal non-invasive imaging in vitro and in vivo monitoring degradation of PLGA scaffold based gold nanoclusters, Mater. Sci. Eng. C. Mater. Biol. Appl. 107 (2020), 110307.